Chapter 4

# Measurement of the Electrical Resistivity for Unconventional Structures

Lucian Pîslaru-Dănescu and
Lipan Laurențiu Constantin

Additional information is available at the end of the chapter

http://dx.doi.org/10.5772/67854

**Abstract**

This study presents an apparatus for the measurement of the electrical volume resistivity of concrete structures in civil and industrial constructions in 2.5 accuracy class, which operates at 500 Hz, for measuring the in situ resistivity of concrete in the range of 5–100 Ωm that is immune to errors due to the polarization phenomena at the interface probe/concrete sample. Also, a quench protection active system (QPS), which works in tandem with a superconducting coil structures (SCSs), in order to prevent the damaging effects when the coil structures pass from the superconducting state into normal conduction state (quench), is presented. An SCS made of YBCO tape high-temperature superconductor (HTS) type, with a critical temperature of 92 K, has been experimented. In order to minimize the heat transfer influx by convection, the SCSs are confined to a cryostat, which is vacuumed at about 0.001 mbar. The working temperature of the HTS coil structures is about 77 K, ensured by liquid nitrogen as cryogenic agent. Finally, the measurement of the electrical resistance of the sensing element (SE) as part of the resistive-type gas sensor is shown. The SE is placed on a Wheatstone bridge. The electrical resistance of the SE is variable by an amount $\Delta R$, on when all the resistances of a Wheatstone bridge are nominally equal.

**Keywords:** electrical resistivity, reinforced concrete structures, coil structures of superconducting, quench protection, sensing element, gas sensors

## 1. Measurement of the electrical resistivity of concrete structures

Measurement of the electrical volume resistivity of concrete structures in civil and industrial constructions shows a particular importance in order to establish the status thereof. In practice, often, it counts the problem of investigating the degradation of reinforced concrete that was not provided with electrodes for monitoring. The degradation of reinforced concrete structures

is a complex process concerted and synergy action due to several requests for the nature of the physical (mechanical stress, shock and vibration, weather air/diurnal temperature variations, especially around the freezing temperature of water, etc.), chemical (salinity of the soil and/or of the phreatic water is in contact with the concrete, the content of aggressive atmospheric pollutants, etc.) and microbiological (load microbiological alteration of the exploitation environment). Measurement of the electrical volume resistivity of concrete structures can be achieved by using a quadrupole consisting of the power electrodes, $E1$, $E2$, by means of which $I$ [A], the current and the measurement electrodes, $E3$, $E4$, to measure a potential difference, $\Delta V$ [V], are injected (**Figures 1** and **2**). An apparent resistivity [1] $\rho_{app}$ [Ωm] is obtained

$$\rho_{app} = \frac{k \times \Delta V}{I} \tag{1}$$

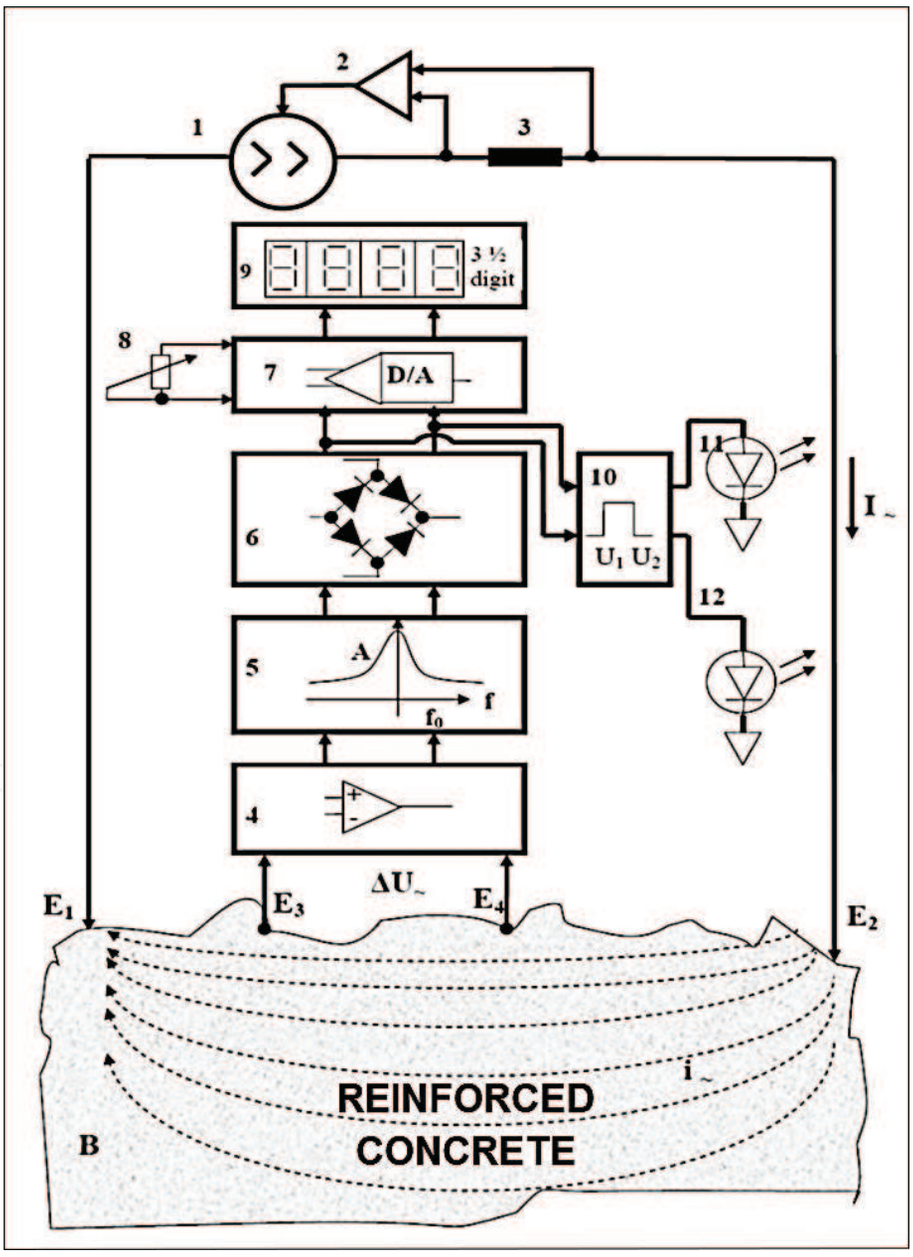


**Figure 1.** The block diagram of the measurement apparatus of the in situ electrical resistivity of concrete structures.

http://dx.doi.org/10.5772/67854

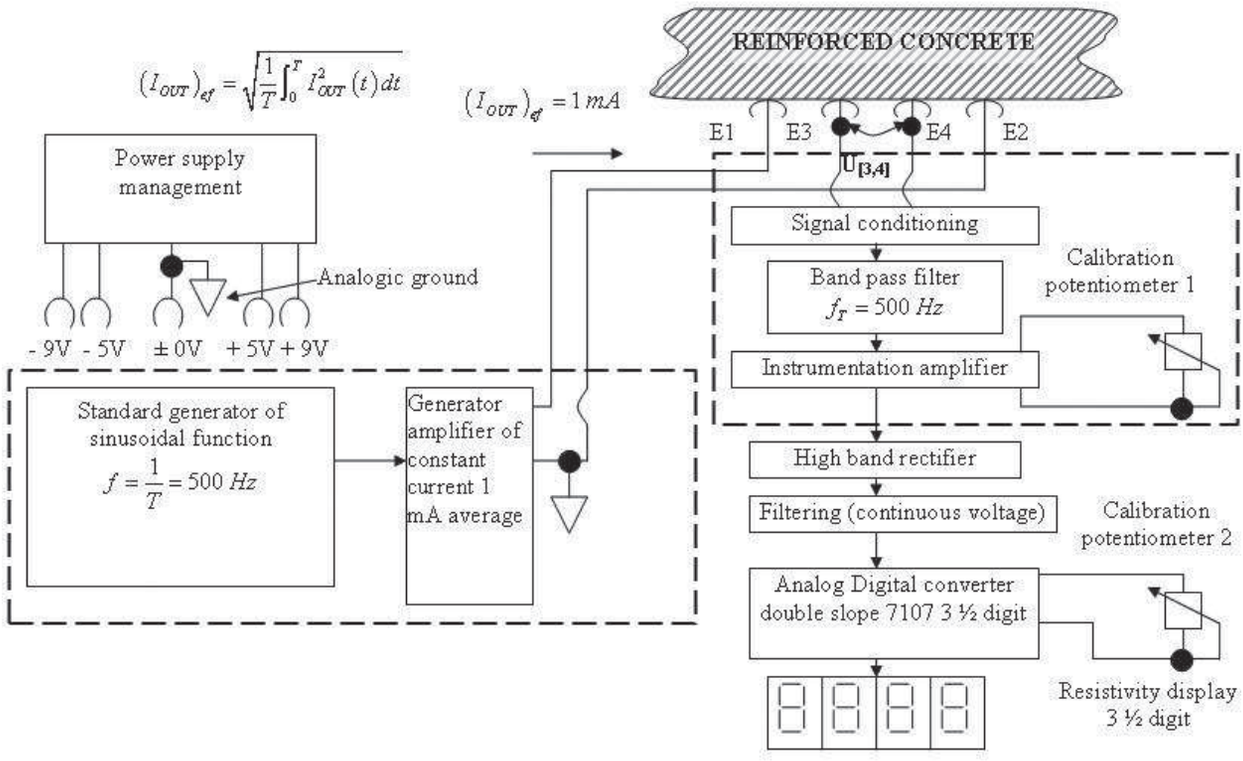


**Figure 2.** The functional modules of the measurement apparatus of the in situ electrical resistivity of concrete structures [7].

Here, $k$ is a sample-specific geometrical factor and $I$ [A] is the injected current. In this case, the RMS value of the injected current is 1 mA. Based on the technical solutions protected by patent application [2], we prototyped an apparatus for measuring the in situ resistivity of concrete structures.

Measurement apparatus of the in situ electrical resistivity of concrete structures is conceived modularly having as components the following electronic modules, as shown in **Figures 1** and **2**: constant current generator module positions 1, 2 and 3, signal conditioning module position 4, band-pass filter position 5, rectifier module position 6, measurement and display module positions 7–9, and window comparator module positions 10–12 [2–6]. The errors due to electrochemical polarization phenomena are eliminated by powering the current electrodes $E1$, $E2$ with a constant of 1-mA intensity sinusoidal current [6], of 500 ± 5 Hz. The constant current generator module is made by cascading the standard generator sine function sub-module and of constant voltage/current converter sub-module of 1 mA RMS. Accompanying the current flow through the concrete sample, a voltage drop of *approx*. $\Delta U$ proportional to the resistivity of concrete, $\rho$, is recorded at the central contacts of the concrete sample, $E3$ and $E4$.

The measuring probe is of special construction, so as to ensure the parallelism of the electrodes $E1$–$E4$, **Figures 1** and **2** and equal distance between them. The concept of the measuring probe allows easy manoeuvrability in the field, regardless of the orientation of the measuring plane (horizontal, vertical walls and beam-reinforced concrete) and simultaneously uniform pressing of the electrodes and even on surfaces with dislevelments up to 15 mm. In order to ensure as good as possible constant electric contact between

electrodes *E*1–*E*4 and the measured concrete structures surface, they are provided with sponge patches capped by cotton cloth discs (protective bags attached to the electrodes by snap rings). To eliminate the errors due to both AC and DC stray currents, low and high frequency, the signal $\Delta U$ at *E*3, *E*4 electrodes is passed through a 'band-pass' filter of 500 ± 10 Hz [3] (with minimum 40-dB attenuation for ±150 Hz).

One of the important electronic modules is the active fourth-order band-pass filter. The band-pass filter is made by cascading a second-order active band-pass Bessel filter with a second-order active band-pass Butterworth filter. Both filters are realized with the use of the Texas Instruments integrated active filters UAF42 [3]. Bessel and Butterworth second-order band-pass filter design was made by using software program FilterPro™ developed by Texas Instruments Company dedicated to developing applications for the integrated circuit UAF42 Texas Instruments—active filter.

With notations required by Texas Instruments, the values of the passive components are obtained from **Table 1** for the second-order Bessel band-pass filter and from **Table 2** for second-order Butterworth band-pass filter, by running the software program FilterPro™.

It can be noted, **Figures 3** and **4**, that the integrated active filter circuit UAF42 [3] contains an operational amplifier unused for filtering function. This is used to achieve signal conditioning, the amplification after filtration, respectively.

The electronic design of the second-order Bessel band-pass filter is shown in **Figure 3**, and the electronic design of the second-order Butterworth band-pass filter is shown in **Figure 4**.

Input voltage of the signal conditioning electronic block is sinusoidal, having amplitude peak to peak in the range of 10–20 mV, recorded at the central contacts of the concrete sample, *E*3 and *E*4, **Figure 2**. This voltage is amplified to the level of 500–1000 mV peak to peak, by using the fourth operational amplifier available into the integrated circuit UAF 42 Texas Instruments—active filter, **Figure 3**, used in the inverting connection. In this case, the gain, as the ratio of the output voltage at this operational amplifier (i.e. from input of the second-order Bessel filter) and the input voltage at the inverting connection of the operational amplifier, **Figure 3**, can be written as

$$A_1 = \frac{V_{OUT1}}{V_{IN1}} = -\frac{R_A}{R_B} = -\frac{100}{2} = -50 \tag{2}$$

| $f_0$ [Hz] | $R_{2A}$ [kΩ] | $R_{F1}$ [kΩ] | $R_{F2}$ [kΩ] | $C_{1A}$ | $C_{2A}$ | $R_Q$ [kΩ] |
|---|---|---|---|---|---|---|
| 500 | 5.49 | 100 | 100 | – | – | 34.8 |

**Table 1.** The values of the passive components for the second-order Bessel band-pass filter.

| $f_0$ [Hz] | $R_{2A}$ [kΩ] | $R_{F1}$ [kΩ] | $R_{F2}$ [kΩ] | $C_{1A}$ | $C_{2A}$ | $R_Q$ [kΩ] |
|---|---|---|---|---|---|---|
| 500 | - | 316 | 316 | – | – | 4.75 |

**Table 2.** The values of the passive components for the second-order Butterworth band-pass filter.

http://dx.doi.org/10.5772/67854

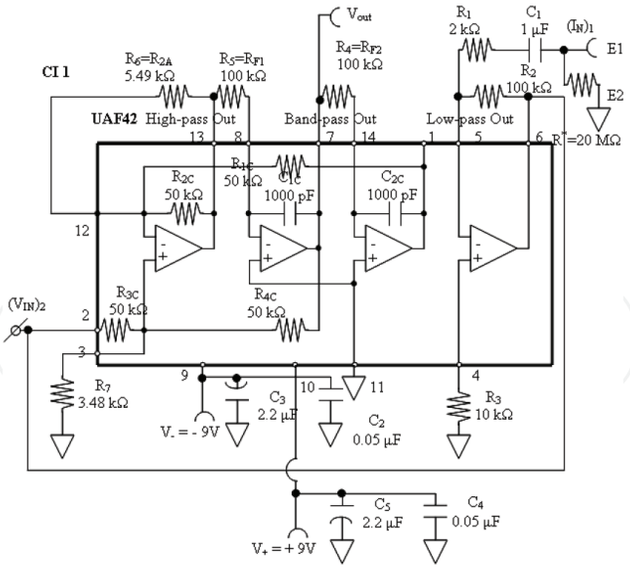


**Figure 3.** The second-order active band-pass Bessel filter and signal conditioning.

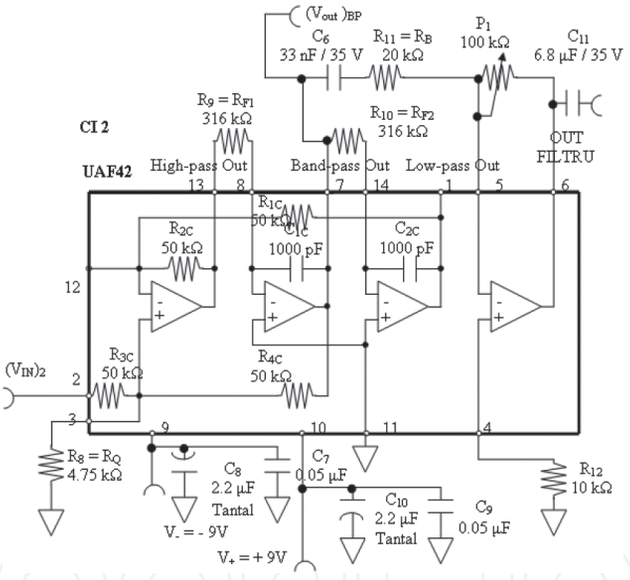


**Figure 4.** The second-order active band-pass Butterworth filter and instrumentation amplifier.

Input voltage from the second-order active filter Butterworth is sinusoidal, having maximum amplitude peak to peak of 1000 mV. The filter is active, so that the maximum output voltage amplitude is the same, 1000 mV peak to peak. This voltage is amplified to the level of 5000 mV peak to peak by using the fourth operational amplifier available into the integrated circuit UAF 42 Texas Instruments—active filter, **Figure 4**, used in the inverting connection. In this case, the gain, as the ratio of the output voltage at this operational amplifier and the input voltage at the inverting connection of the operational amplifier, **Figure 4**, can be written as

$$A_2 = \frac{V_{OUT2}}{V_{IN2}} = -\frac{P_1}{R_B} = -\frac{100}{20} = -5 \tag{3}$$

Experimentation of the second-order band-pass active filter Bessel was performed as follows:

- at the input of the second-order band-pass active filter Bessel, **Figure 3**, a sinusoidal voltage with a peak-to-peak amplitude of 1000 mV and a frequency range of $f$ = 50–1000 Hz, from the arbitrary function generator FLUKE 281, was applied;
- the output of band-pass filter Bessel is connected to the LeCroy 324 digital oscilloscope channel 1, in order to measure the amplitude of the output voltage;
- by using the entire spectrum of the frequencies, in the range of $f$ = 50–1000 Hz, for the sine wave voltage applied to the input, the characteristic of the second-order band-pass active filter Bessel, **Figure 5**, can be drawn.

Experimentation of the second-order band-pass active filter Butterworth was performed as follows:

- at the input of the second-order band-pass active filter Butterworth, **Figure 4**, a sinusoidal voltage with a peak-to-peak amplitude of 1000 mV and a frequency range of $f$ = 50–1000 Hz, from the arbitrary function generator FLUKE 281, was applied;
- the output of band-pass filter Butterworth is connected to the LeCroy 324 digital oscilloscope channel 2, in order to measure the amplitude of the output voltage;
- by using the entire spectrum of the frequencies, in the range of $f$ = 50–1000 Hz, for the sine wave voltage applied to the input, the characteristic of the second-order band-pass active filter Butterworth, **Figure 6**, can be drawn.

The fourth-order filter, obtained by cascading the two second-order filters, Bessel and Butterworth, was tested in the same conditions. The characteristic of the fourth-order band-pass active filter is shown in **Figure 7**.

In order to eliminate the measurement error due to the polarization phenomena between the reinforced concrete surface (conductor environment of type II) and the electrodes $E1$, $E2$

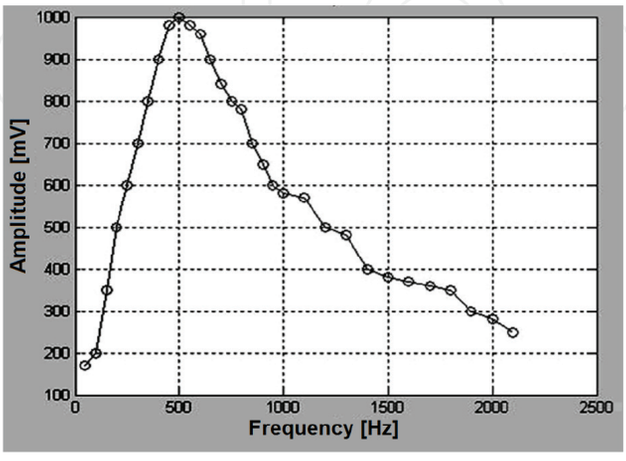


**Figure 5.** The characteristic of the second-order band-pass active filter Bessel (two poles), test results [7].

http://dx.doi.org/10.5772/67854

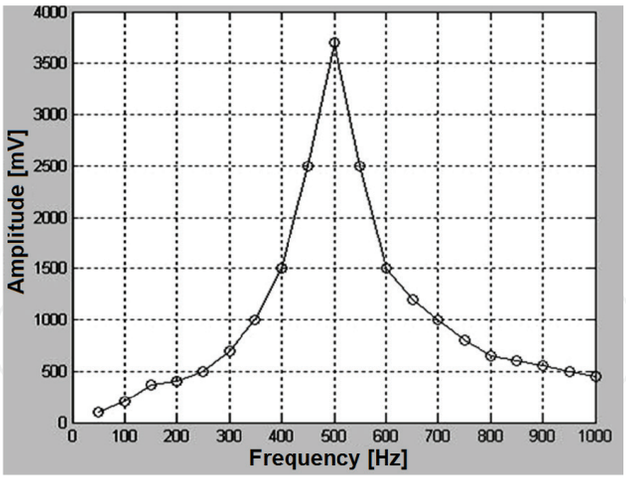


**Figure 6.** The characteristic of the second-order active band-pass filter Butterworth (two poles), test results [7].

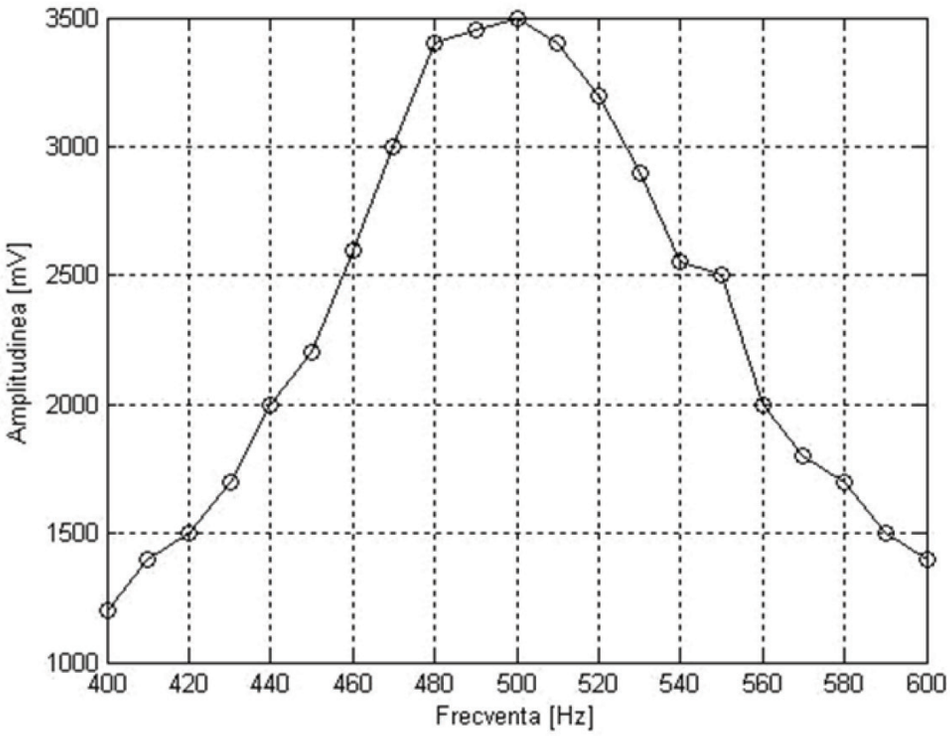


**Figure 7.** The characteristic of the fourth-order band-pass active filter (four poles), for the frequency of 400–600 Hz, resulted by cascading the two second-order Bessel and Butterworth filters, test results.

(conductor environment of type I), the apparatus includes the current generator module, made by cascading the standard generator sine function sub-module of 500 ± 5 Hz and of constant voltage/current converter sub-module of 1 mA RMS.

In order to eliminate the measurement error due to the potential leakage currents both in DC and in AC, of low and high frequency, and of the interference signals, respectively,

with frequencies below 350 Hz and above 1 kHz, the apparatus includes the fourth-order band-pass active filter made by cascading the two second-order band-pass active filter modules Bessel and Butterworth filters. As I pointed out, the apparatus for the measurement of the electrical volume resistivity of concrete structures in civil and industrial constructions provides the measurements of resistivity in the range of 5–100 Ωm, the 2.5 accuracy class. By using a window comparator electronic module, **Figure 1**, the apparatus allows the optical viewing of the values less than 5 Ωm and over 100 Ωm, through two leads. The apparatus shows the good functional stability, observed during experiments for a wide range of types of concrete structures. Also, the calibration can be done easily by using a potentiometer P1, **Figure 4**.

As concrete structures degrade (through decrease of the alkalinity, carbonation, increase in chloride content, etc.), the resistivity decreases substantially [8]. Today at important buildings, from design phase is provided embedding electrodes that allowing both measuring/monitoring of the concrete resistivity and determination of the potential of corrosion of the reinforcement [9–11].

Experiments were performed in two stages.

*Stage 1. Calibration*

Standard concrete sample (SCS) for which precisely the electrical resistivity is known, determined by the classical method [12], is measured in order to calibrate the apparatus:

(A1) it is checked using a 'TRUE RMS AC + DC' multimeter set on the mA scale and having probes connected to *E*1 and *E*2 electrodes, respectively, that RMS value of the injected current is to 1 mA;

(B1) the sponge and protective bag for probes (up to saturation) are soaked with a solution of 3–5% NaCl concentration;

(C1) the electrodes *E*1–*E*4 are applied on the SCS sample surface;

(D1) the measurement apparatus of the in situ electrical resistivity of concrete structures is calibrated, through adjusting the amplification of the instrumentation amplifier, by rotating the calibration potentiometer on the front panel, **Figures 1** and **2**, until the apparatus indicates the known resistivity value of the SCS sample.

*Stage 2. Measuring the electrical resistivity of concrete structures*

(A2) before performing a new measurement, the sponge and the protective bag are soaked again (to saturation) with a solution of 3–5% NaCl concentration;

(B2) the electrodes *E*1–*E*4 are applied on the concrete structure surface;

(C2) the measured value of the electrical resistivity of concrete structures is read on the digital display of 3 1/2 digits.

**Figures 8** and **9** present two successive measurements of resistivity of a concrete pillar.

http://dx.doi.org/10.5772/67854


**Figure 8.** The measurement of a concrete pillar, first measurement.

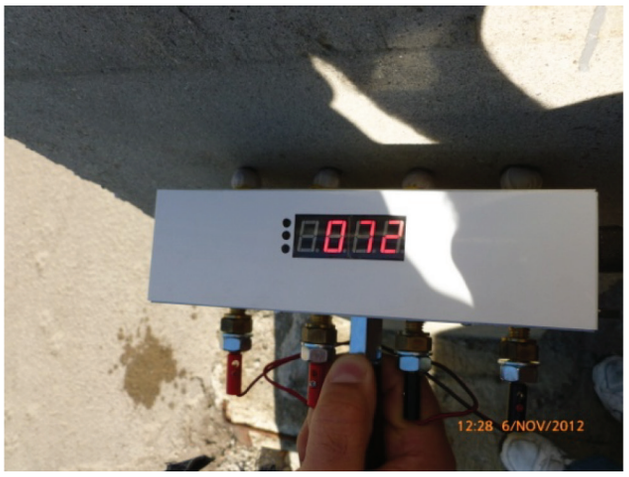


**Figure 9.** The measurement of a concrete pillar, second measurement.

## 2. Protection to quench hazard in high-temperature superconducting coil structures

### 2.1. The case of a single HTS superconducting coil

The superconducting coil structures can get out of the superconducting state (can normalize), for various reasons, such as the following:

- if temperature exceeds the critical temperature;
- if the injected current growth slope is too steep, after entering the superconducting coil structures in the superconducting state and stabilizing to the temperature regime at a value of 77 K (liquid nitrogen temperature);

- if the injected current through the superconducting coil structures exceeds the critical current;
- if the superconducting coil structures are subjected to mechanical vibrations [13].

Therefore, the superconducting coil structures always work in tandem with a protection system, called quench protection, in order to prevent the damaging effects of their exit from the superconducting state, for the reasons previously described.

This study refers to the quench protection active system (QPS), which works in tandem with a superconducting coil structure. In our case, the superconducting coil structures are made from a tape of material based on YBCO, having a critical temperature of 92 K. Since cooling is made with liquid nitrogen, the working temperature of the superconducting coil structures is in the temperature range of 77 K. The superconducting coil structures are arranged in a cryostat within which a high vacuum of about 0.001 mbar is achieved, in order to minimize the heat transfer to the outside by removing the convective heat transfer. Also, the superconducting coil structures are immersed in liquid nitrogen. **Table 3** presents the electrical resistance of the superconducting coil structures versus the cryostat temperature.

At the critical temperature, the resistance of the coil temperature ensemble is 0.52 Ω (superconducting coil resistance to which the connecting wire resistance and the junction resistance are added). All the connecting wires are made of superconducting material YBCO, HTS type that has a thermal conductivity of ~1 W/mK. The connecting wires are introduced in a sheath of nonmagnetic stainless steel pipe and the terminals are made by copper. Bonding the HTS strip of copper terminals is carried out with a mixture of indium and 5% Ag (to minimize the junction resistance).

**Figure 10** presents the variation of the voltage measured on the superconducting coil structures after entering into the superconducting state, depending on the injected current. The

| **Temperature in the cryostat *T* [K]** | **The measured resistance of the superconducting coil *R* [Ω]*** |
|---|---|
| 119 | 0.58 |
| 114 | 0.55 |
| 104 | 0.52 |
| 84 | 0.517 |
| 77.6 | 0.495 |
| 77.54 | 0.465 |
| 77.52 | 0.452 |
| 77.51 | 0.44 |
| 77.53 | 0.434 |
| 77.46 | 0.43 |

*The superconducting coil structures resistance was measured in the conditions in which no current was injected in the coil.

**Table 3.** The electrical resistance of the superconducting coil structures versus the cryostat temperature.

http://dx.doi.org/10.5772/67854

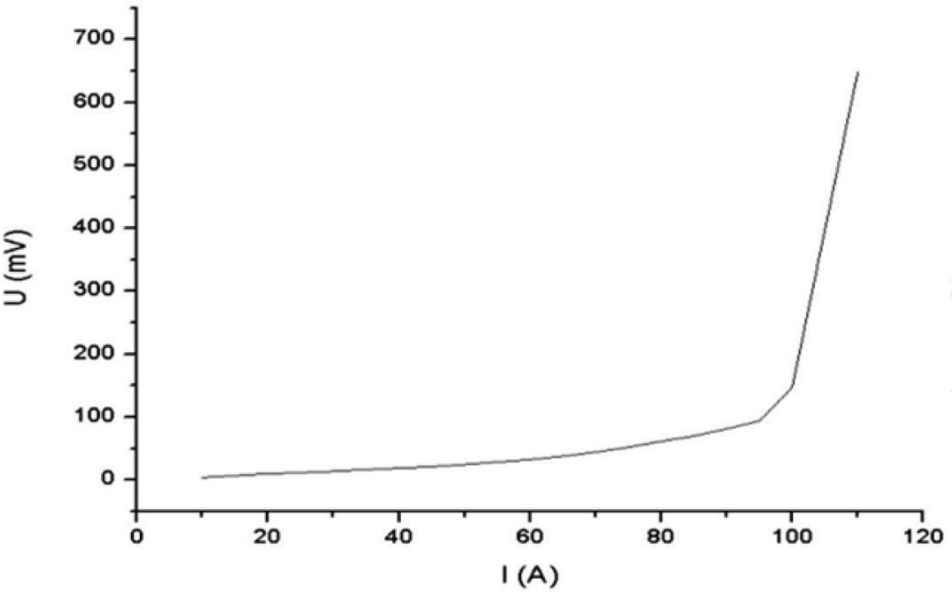


**Figure 10.** The voltage drop on the superconducting coil structures versus the current, at 77 K [14].

current is injected through the superconducting coil structures, with a slope of 1 A/s [14] by the programmable power supply type AMI 03300PS-430-601. Critical current value is determined from the curve $U = f(I)$, **Figure 10**, by coming down with a tangent at exponential area of the curve. The value of the critical current was determined using this procedure and it is 120 A. The intersection with current axis, **Figure 10**, will give the exact value of critical current of the superconducting coil structures at 77 K. For a current greater than or equal to the critical current, the voltage measured on the superconducting coil structures has a sudden increase. The superconducting coil structures get out of the superconducting state, and the quench protection must act accordingly in order to prevent the damaging effects.

The quench protection system (QPS) is made of two ultrafast switches made with high-power IGBT's transistors (Isolate Gate Bipolar Transistor). The key parameters of the active protection system are as follows:

- The maximum quench detection time is $t_Q$ = 800 ns;
- The actual reaction time is in the interval $t_R$ = 2.78–3.5 μs;
- The energy is discharged in the range of 1–10 kJ.

A quench active protection system, **Figure 11**, for HTS coil structures must solve the following problems:

1. The detection of the QUENCH.
2. Decoupling the HTS coil structures from the programmable power supply.
3. The coupling of the HTS-type superconducting coil structures on a discharge resistance $R_D$. In this case, the magnetic energy stored in the coil inductivity $L$, $W_M = Li^2/2$, is dissipated through Joule effect, $W_J = Ri^2$, by the discharge resistance $R_D$ and the dynamic resistance of the semiconductor device that compose the command power electronic switch.

To comply with its aim, the quench protection active system, **Figures 11** and **27**, must comprise the following parts: ultrafast electronic switches, $T1$ and $T2$ ($K1$ and $K2$, respectively), an electronic circuit for quench detection and a discharge resistance, $R_D$.

The design of the quench protection system (QPS) is modular, and it comprises the electronic modules presented next.

**A.** Quench detection and signal processing electronic module. This module, named **1**. on the **Figure 11**, contains the following parts:

- An operational amplifier electronic block with galvanic isolation;
- A precision, differential amplifier electronic block with the common mode rejection factor $CMRR$ = 100 dB;
- An amplifier electronic block with the gain $A$ = 10 and $CMRR$ = 100 dB;
- An electronic block, which performs the module mathematical function;
- An optical interface electronic block, double opto-coupler, with TTL signals recovery;
- A logic sequence programming electronic block.

**B.** The power electronic module. This module, named **2**. on the **Figure 11**, comprises the following electronic blocks:

- Two drivers electronic blocks IGBT T1/IGBT T2 (Block 1 Driver IGBT T1 and Block 2 Driver IGBT T2);
- An electronic block of ultrafast switches made with the power transistors IGBT T1/IGBT T2;
- A discharge resistance block, $R_D$.

**C.** Electronic module of voltage stabilized power supplies. This module, named **3**. on the **Figure 11**, comprises the following blocks:

- The ±12 $V_{DC}$ differential power supply for powering the analogical electronic circuits and the power supply +5 $V_{DC}$ for powering the digital electronic circuits;
- The ±15 and ±12 $V_{DC}$ differential voltage power supply for powering the operational amplifier electronic circuit with optical isolation for the quench signal processing;
- The 2x20 $V_{DC}$ power supply with galvanic isolation for powering the drivers that command the two IGBT power transistors, $T1$ and $T2$.

The discharge resistance $R_D$, **Figures 11** and **12**, was made from 99.9% pure Cu wire, solenoid shape, having four turns with section $\Phi$ = 2 mm, with the wire diameter of $D$ = 50 mm, and the value of the DC resistance of $R_D$ = 0.128 Ω. The DC measurement was performed with the Agilent 34461A multimeter.

One of the important electronic modules is the amplifier block with galvanic isolation. Design of the amplifier block with galvanic isolation, **Figure 13**, is made with the integrated circuit

http://dx.doi.org/10.5772/67854

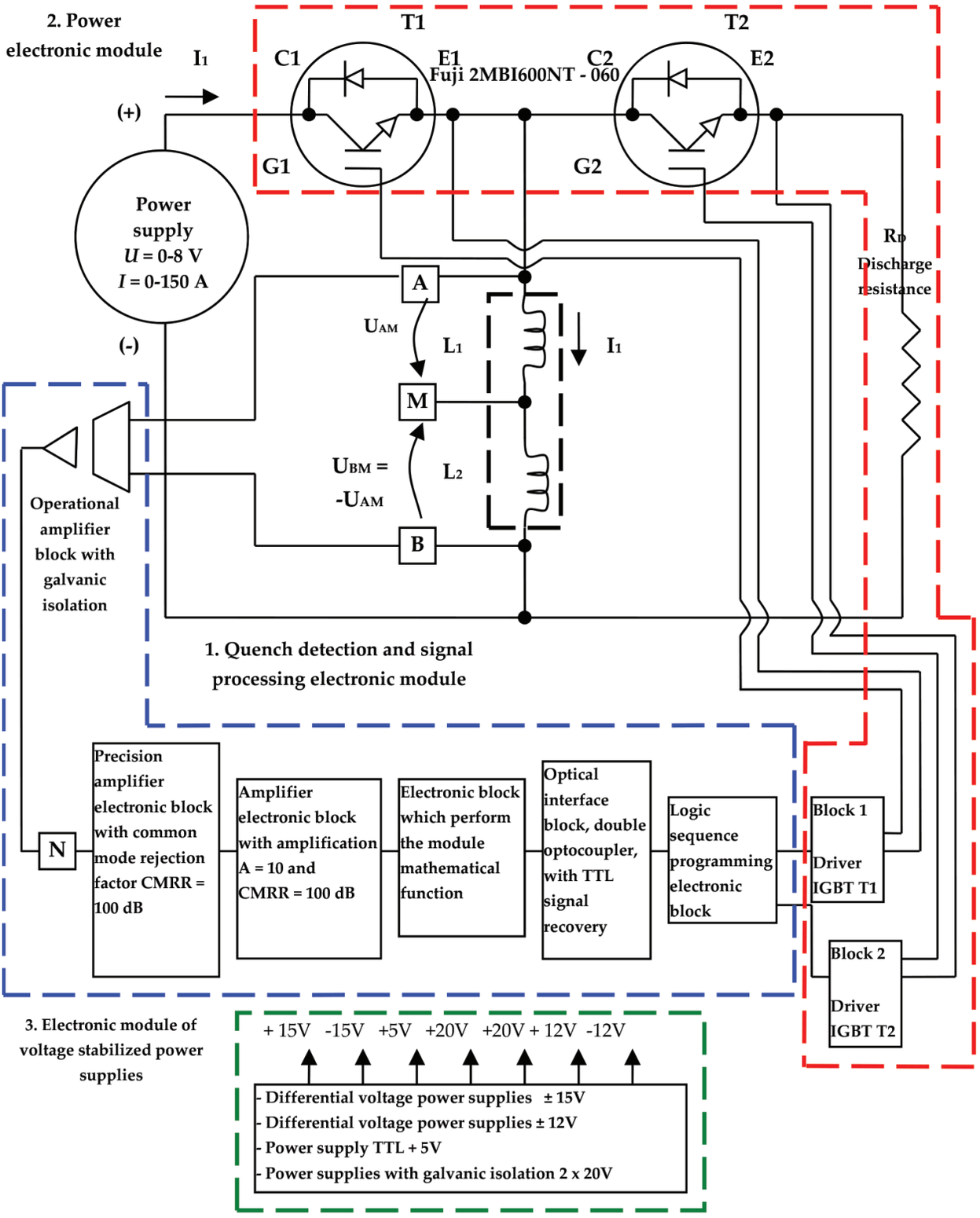


**Figure 11.** The block diagram of the experimental model of the QPS, which provides the HTS coil structures protection to quench, for the case of a HTS coil [14].

IC1 type ISO 124, Burr Brown manufacturing by Texas Instruments. It is noticed that the useful signal is acquired through a divider, made with four potentiometers *P*1–P4, respectively.

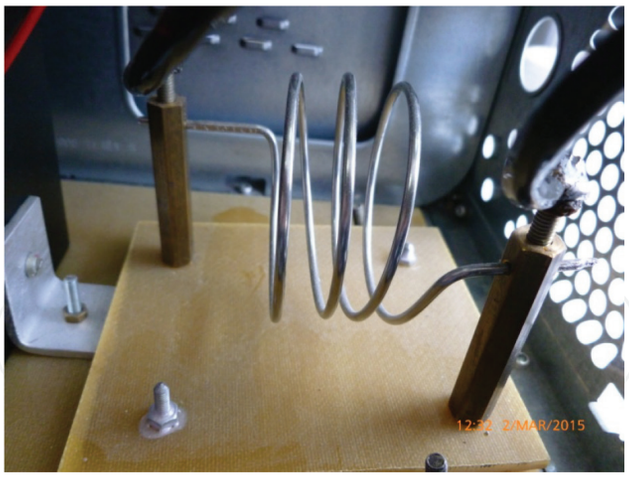


**Figure 12.** The discharge resistance $R_{D.}$

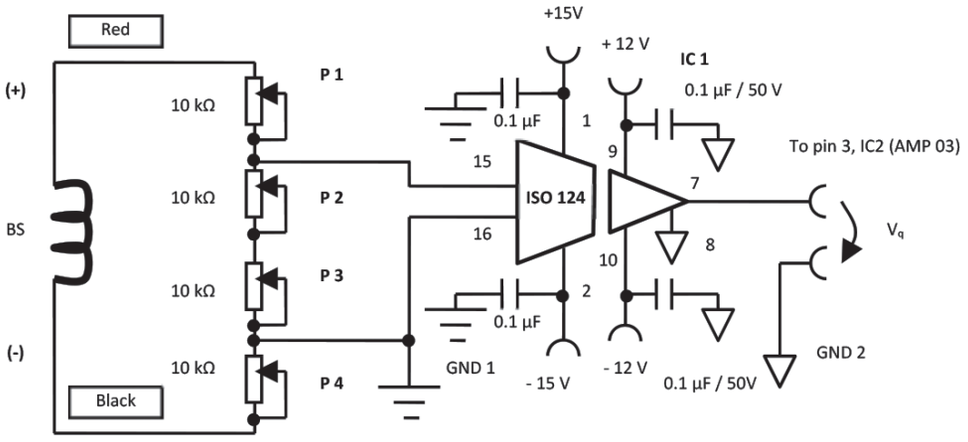


**Figure 13.** The electronic design of the amplifier block with galvanic isolation [14].

In this way, the dividing factor is adjustable allowing the useful signal threshold setting for which the voltage of the amplifier input is interpreted as quench voltage. Also, it can be seen the separation way of the power supply, **Figure 13**. A differential stabilized power supply of DC voltage of ±15 $V_{DC}$, which is powering the first part of the amplifier block with galvanic isolation type ISO 124, which acquires the useful signal and a differential stabilized power supply of DC voltage of ± 12 $V_{DC}$, which is completely galvanic isolation from first is powering the part of the output amplifier.

The power electronic module of the active electronic protection system QPS contains two electronic ultrafast switches made with the power transistors IGBT T1/IGBT T2 type Fuji 2MBI600NT—060, **Figures 14** and **15**, two drivers electronic blocks IGBT T1/IGBT T2, type VLA 517—01R—FUJI [15] **Figures 16** and **17**, and a discharge resistance $R_D$, **Figures 11** and **12**, with the role of picking the energy stored in a superconducting coil that is composed of two identical sections, serially connected, when at least one of the coils is normalized.

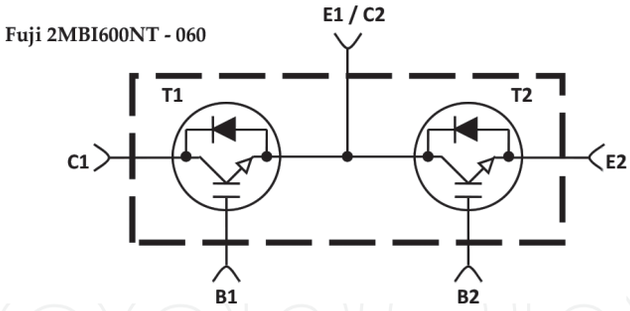


**Figure 14.** The ultrafast switches block made with the IGBT T1/IGBT T2 [14].


**Figure 15.** IGBT power transistors, T1/T2 type 2MBI 600 U2 E—060—FUJI [14].

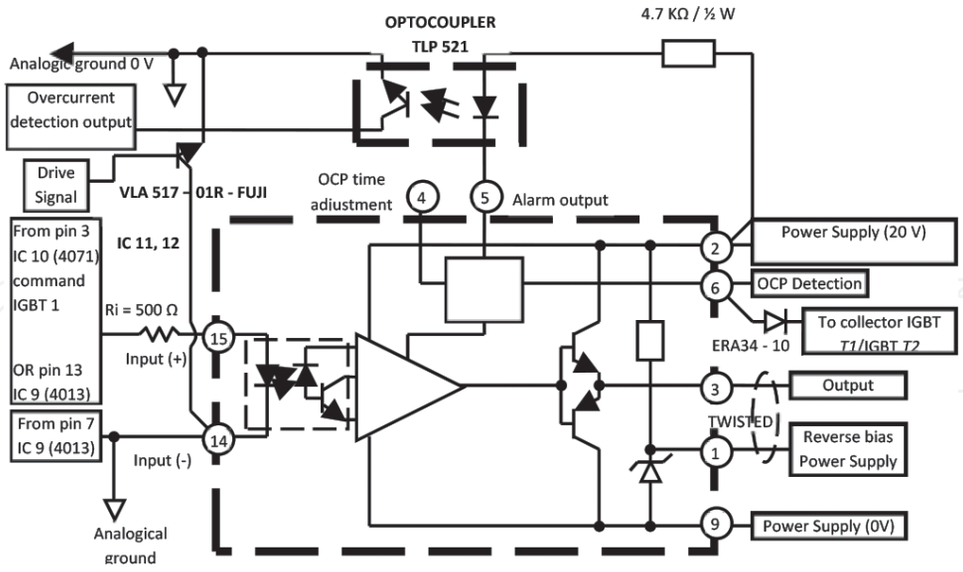


**Figure 16.** The IGBT T1/IGBT T2 driver block [14].

The first ultrafast switch made with the power transistors IGBT T1, **Figures 11** and **18**, allows the supply of the superconducting coil from the voltage power supply, in normal operation, as well as voltage power supply decoupling when the coil is normalized. The second switch


**Figure 17.** Hybrid integrated circuit, type VLA 517—01R—FUJI, driver [14].

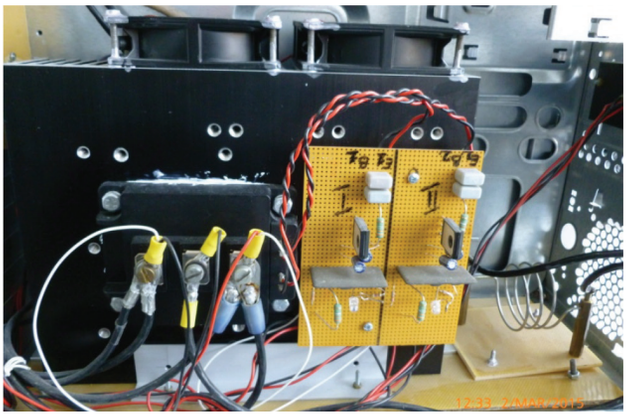

**Figure 18.** The power electronic module of the active electronic QPS system, practical design.

made with the power transistors IGBT T2, **Figures 11** and **18**, enables the coupling of the superconducting coil on the discharge resistance $R_D$, when at least one of the coils $L1$ and $L2$ serially connected is normalized (leaves the superconducting state).

Five possible cases of conduction are distinguished for ultrafast switches made with IGBT power transistors $T1/T2$, according to the conduction state of the two identical sections of superconducting coil $L1$ and $L2$ as follows:

1. Coil inductance $L = L1 + L2$ is in the superconducting state, in which case IGBT power transistor $T1$ is in a state of conduction (ON) and IGBT power transistor $T2$ is found in the locked state (OFF), **Figure 19**;
2. Inductance coil $L1$ was normalized and both IGBT power transistors $T1$ and $T2$ are in a state of conduction (ON) for a period of $t_{M1} = 300$ ns, **Figure 20**;
3. Inductance coil $L1$ was normalized and IGBT power transistor $T1$ is in the locked state (OFF) and IGBT power transistor $T2$ is found in a state of conduction (ON), **Figure 21**;
4. Inductance coil $L2$ was normalized and both IGBT power transistors $T1$ and $T2$ are in a state of conduction (ON) for a period of $t_{M1} = 300$ ns, **Figure 22**;

http://dx.doi.org/10.5772/67854

5. Inductance coil L2 was normalized and IGBT power transistor $T1$ is in the locked state (OFF) and IGBT power transistor $T2$ is found in a state of conduction (ON), **Figure 23**.

The logic sequence programming electronic block, **Figure 11**, performs the following functions:

- Should the coils $L_1$ and $L_2$ work in their superconducting state, in which case the IGBT power transistor $T1$ will be in the conducting state (saturated), and the IGBT power transistor $T2$ is in the locked state. In this case, through the superconducting coil $L = L1 + L2$, **Figure 11** flows the current $I1 = 80$A.
- When the quench phenomenon appears, when at least one of the coils $L1$ or $L2$ is normalized, $V_{COMMAND}$ transits from '0' logic to '1' logic. $V_{COMMAND}$ triggers the voltage $U_{M1}$ over a period $t_{M1}$ and both the IGBT transistors $T1$ and $T2$ are conducting, for a period of $t_{M1} = 300$ ns. In the following sequence, **Figures 24–26**, the IGBT power transistor $T1$ will be in the locked state, and the IGBT power transistor $T2$ will be in the conducting state. Note that the $U_{Q1}$ is the command voltage applied onto IGBT $T1$ and the $U_{Q2}$ is the command voltage applied onto IGBT T2. In this way, the superconducting coil $L = L1 + L2$ will be in parallel with the discharge resistance $R_D$. The magnetic energy accumulated in the superconducting coil $L = L1 + L2$ is dissipated through the protection resistor, discharge resistance $R_D$. The energy is discharged in the range of 1–10 kJ.

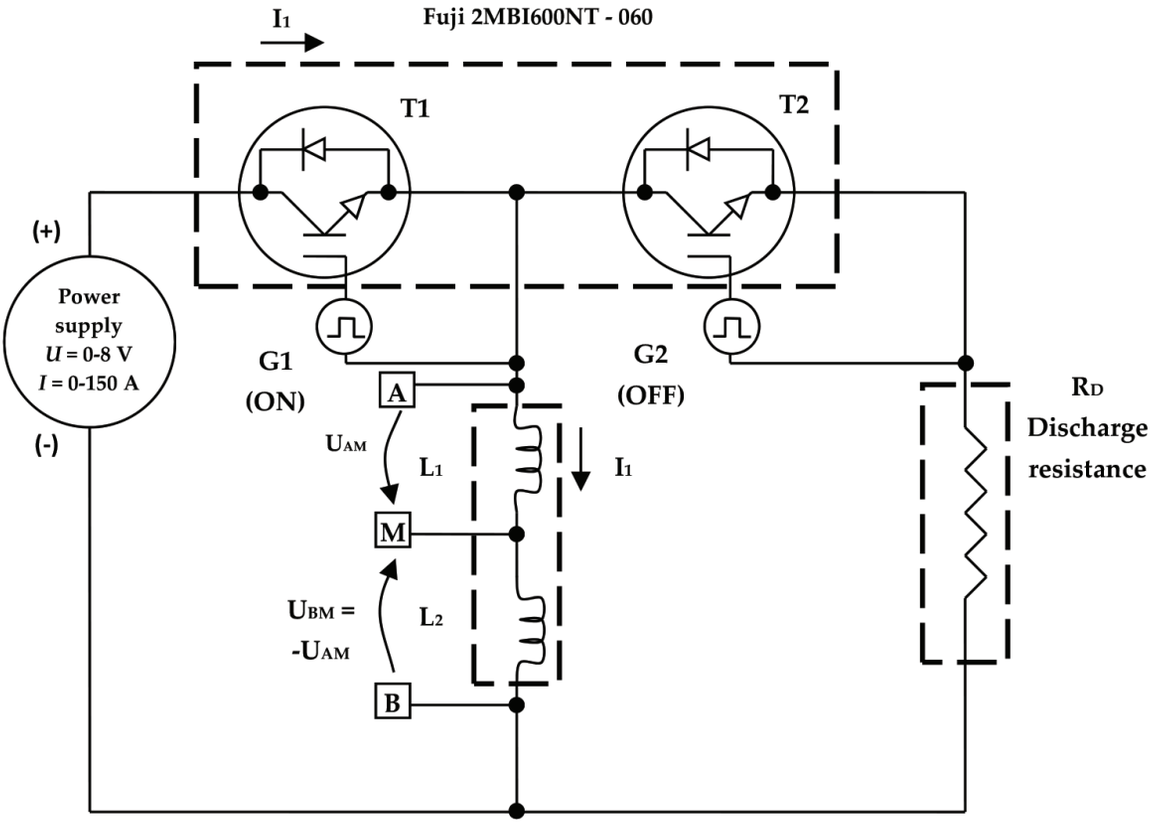


**Figure 19.** Coil inductance $L = L1 + L2$ is in the superconducting state, in which case IGBT power transistor $T1$ is in a state of conduction (ON) and IGBT power transistor $T2$ is found in the locked state (OFF).

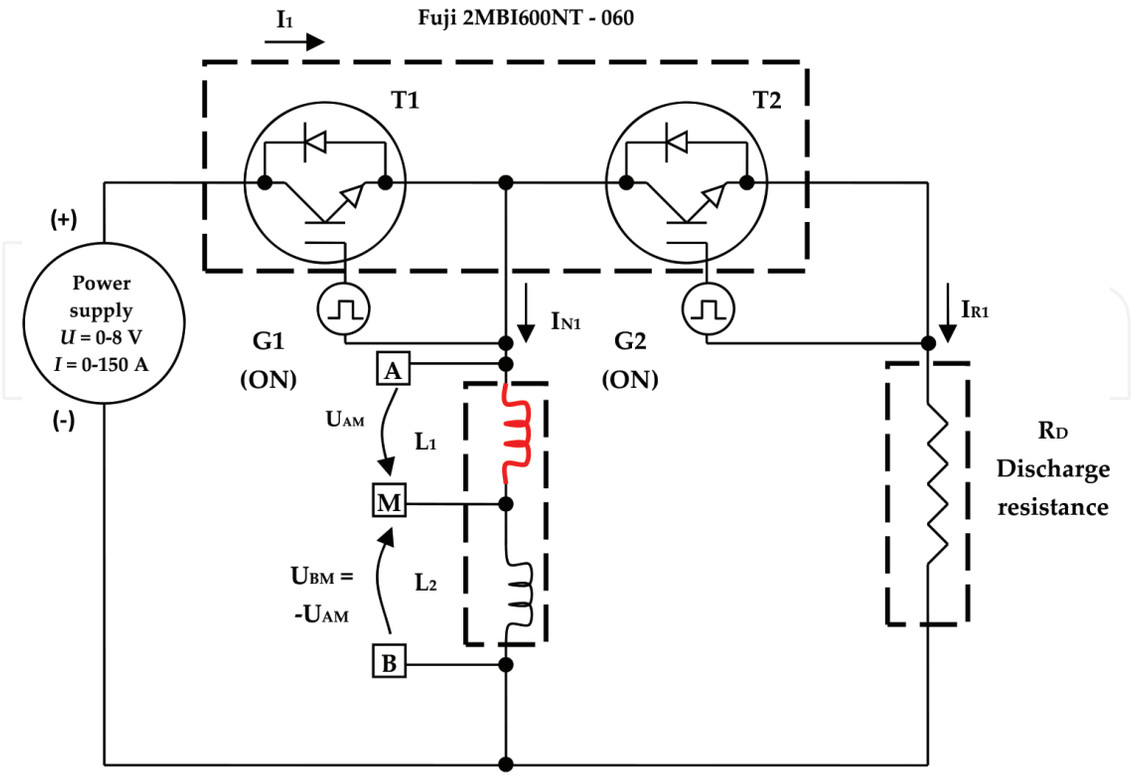


**Figure 20.** Inductance coil $L1$ was normalized and both IGBT power transistors $T1$ and $T2$ are in a state of conduction (ON) for a period of $t_{M1}$ = 300 ns.

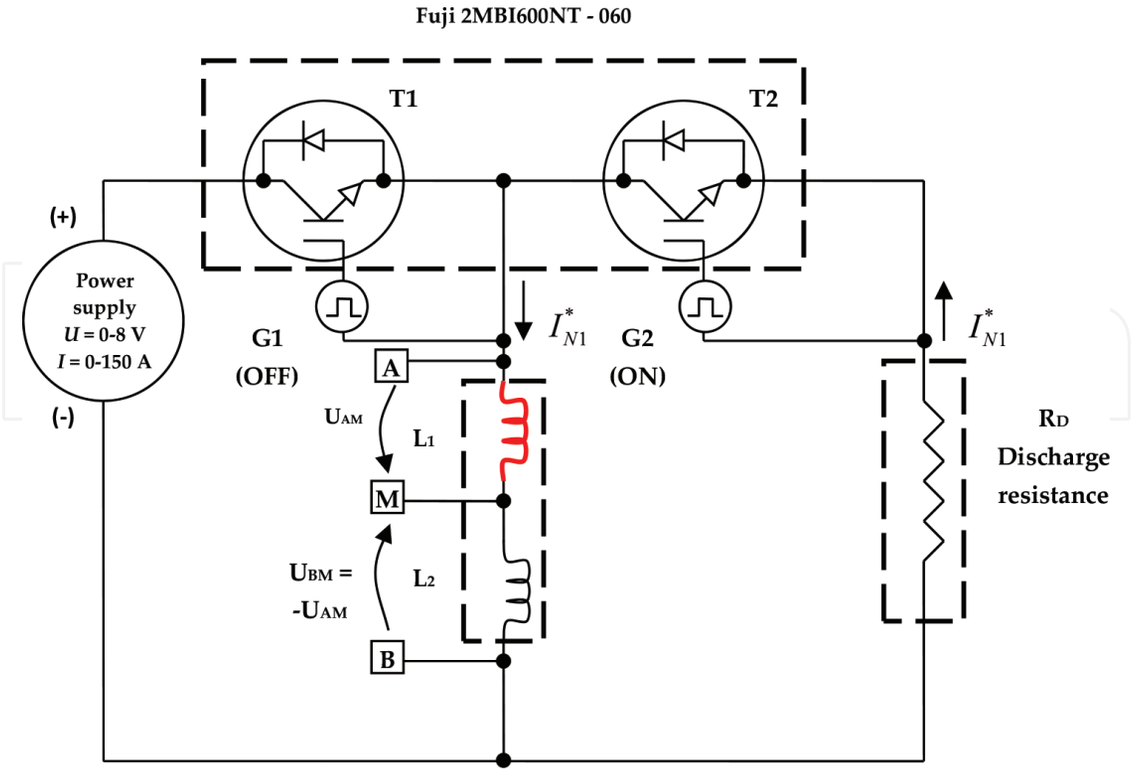


**Figure 21.** Inductance coil $L1$ was normalized and IGBT power transistor $T1$ is in the locked state (OFF) and IGBT power transistor $T2$ is found in a state of conduction (ON).

http://dx.doi.org/10.5772/67854

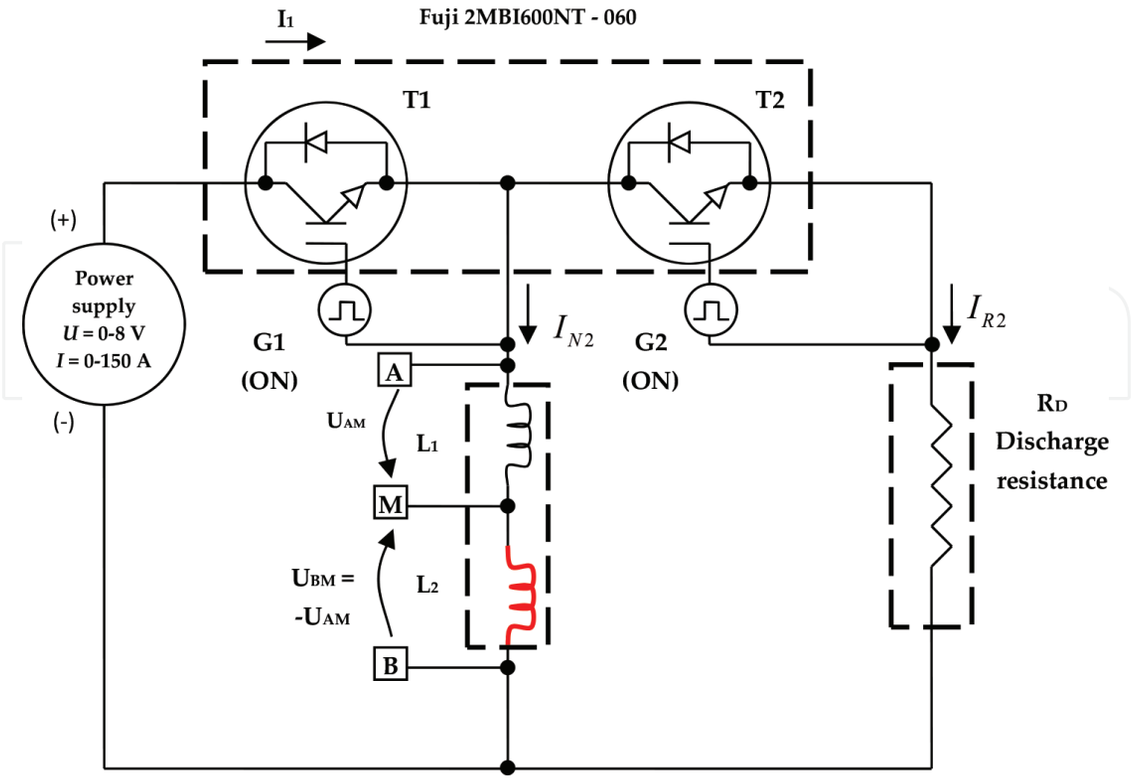


**Figure 22.** Inductance coil *L*2 was normalized and both IGBT power transistors *T*1 and *T*2 are in a state of conduction (ON) for a period of $t_{M1}$ = 300 ns.

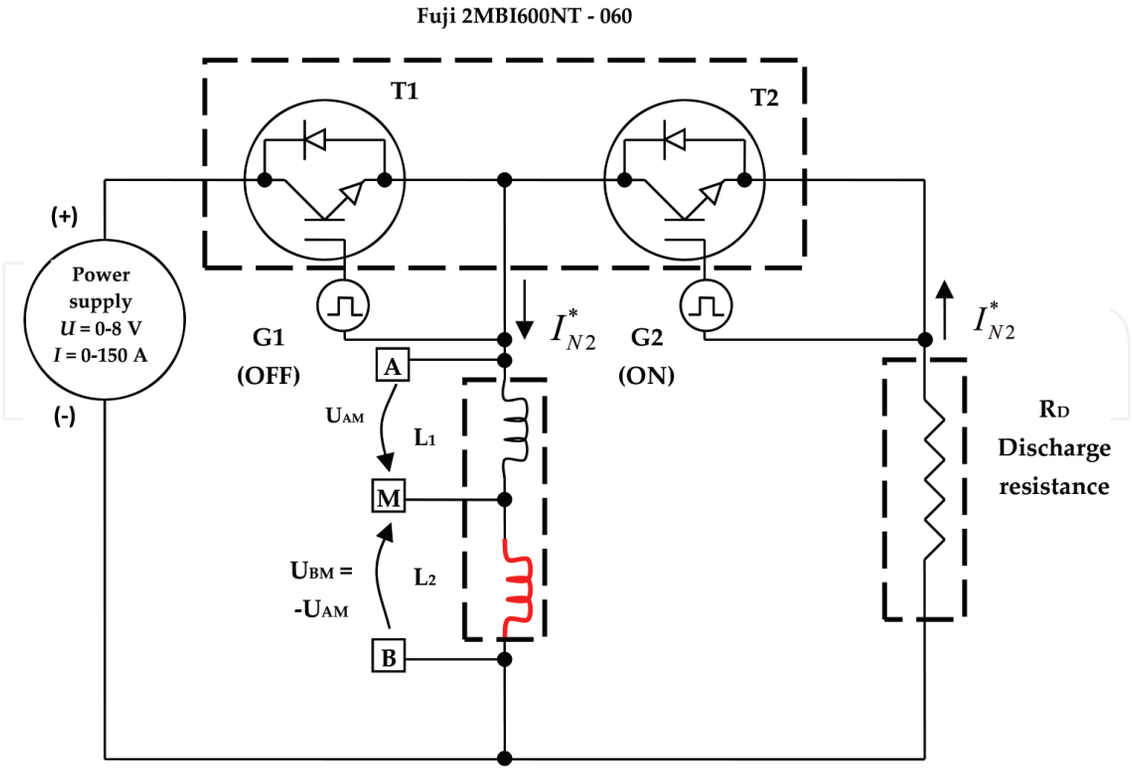


**Figure 23.** Inductance coil *L*2 was normalized and IGBT power transistor *T*1 is in the locked state (OFF) and IGBT power transistor *T*2 is found in a state of conduction (ON).

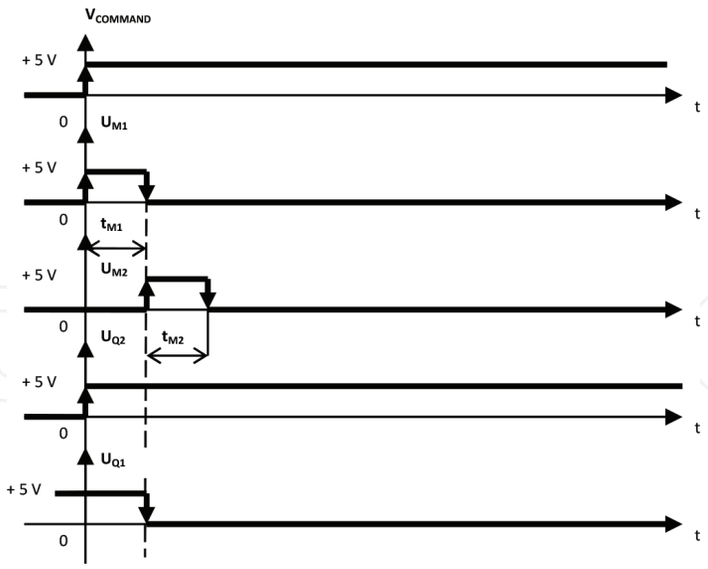


**Figure 24.** The time command diagram of ultrafast switches IGBT T1/IGBT T2, when the quench phenomenon appears [14].

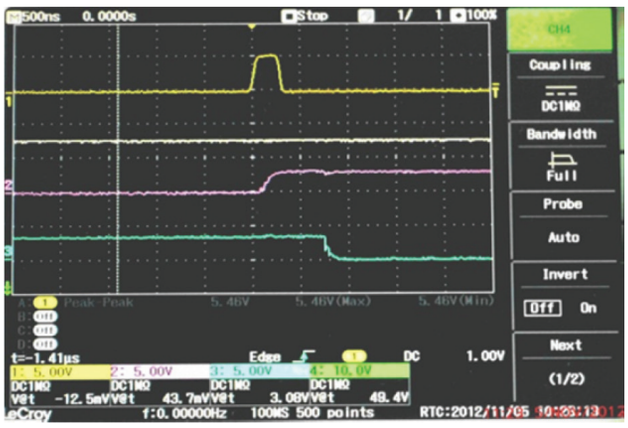


**Figure 25.** Simultaneous recording of signals $U_{M1}$ (overhead), $U_{Q2}$ (in the middle) and $U_{Q1}$ (on the bottom), for a time base set at 500 ns [14].

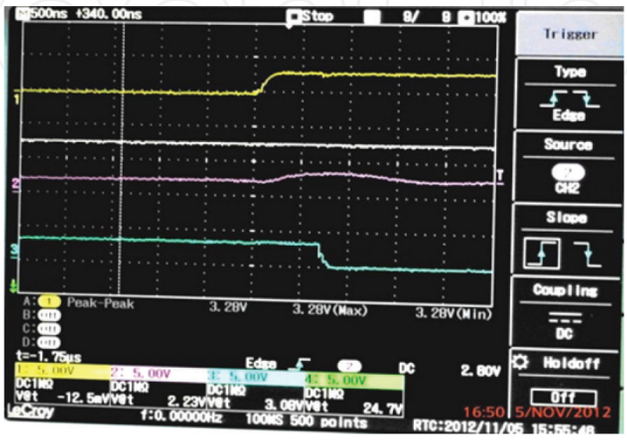


**Figure 26.** Simultaneous recording of signals $V_{COMMAND}$ (overhead), $U_{Q2}$ (in the middle) and $U_{Q1}$ (on the bottom), for a time base set at 500 ns [14].

From **Figures 25** and/or **26**, the maximum quench detection time of the QPS as $t_Q$ = 800 ns can be determined by assessing transition from logic zero to logic one (positive logic) of the signal $U_{Q2}$ or by assessing transition from logic one to logic zero (positive logic) of the signal $U_{Q1,}$ respectively. The reaction time of the QPS, $t_{R,}$ will take into account and by the actual transition from logic zero to logic one (positive logic), '$t_{on}$', for both the command driver's and the IGBT's transistors, respectively. Thus, the transition from logic zero to logic one and transition from logic one to logic zero, respectively, for the driver command type VLA 517—01R—FUJI [15], $t_{on}$-driver = $t_{off}$-driver = $t_{DRIVER}$ = 1.5 μs.

Also, the transition from logic one to logic zero for high-power IGBT transistor type Fuji 2MBI600NT – 060 $t_{off}$-IGBT is determined based on the dispersion of such semiconductor device fabrication: $(t_{off}\text{-}IGBT)_{MIN}$ = 0.48 μs and $(t_{off}\text{-}IGBT)_{MAX}$ = 1.20 μs. The reaction time $t_R$ can be calculated as follows:

(a) The minimum reaction time is

$t_{RMIN} = t_Q + t_{DRIVER} + (t_{off} - IGBT)_{MIN}$ = 0.8 μs + 1.5 μs + 0.48 μs = 2.78 μs.

(b) The maximum reaction time is

$t_{RMAX} = t_Q + t_{DRIVER} + (t_{off} - IGBT)_{MAX}$ = 0.8 μs + 1.5 μs + 1.2 μs = 3.5 μs.

The actual detection time lies in the interval $t_R$ = 2.78–3.5 μs.

Advantages of the QPS [16], which provides the HTS coil structures protection to quench, are as follows:

- Makes a quench detection under quench detection time $t_0$ = 800 ns;
- Makes a decoupling of the power supply, which supplies the superconducting coil through an electronic ultrafast switch, capable of commuting under 1 μs;
- Makes the crossing of the superconducting coil in parallel on a discharge resistance, $R_{D,}$ after the decoupling from the voltage power supply, through an electronic ultrafast switch capable of commuting under 1 μs.

### 2.2. The case of a variable number of HTS superconducting coils, which may form dipolar, cuadripolare, sextupolare or octupolare structures

Active protection for multipolar set of superconducting coils, whose block diagram is given in **Figure 27**, operates in the following way:

Constructively, a multiple number of 2, the superconducting coils 2–8 multipolar BS1, …, BS8 superconducting coils forming the multipole assembly are connected in series. A multiple number of 2, from 2 to 8 electronic amplifiers with galvanic isolation blocks, equal to the number of superconducting coil assembly previously established, BIG1, BIG2, …, BIG8, having the role of individually conditioning the useful signal originated from each superconducting coil in part, are disposed in parallel with each superconducting coil in part, **Figure 27**. The two ultrafast electronic switches, **Figure 27**, *K*1 and *K*2, respectively,

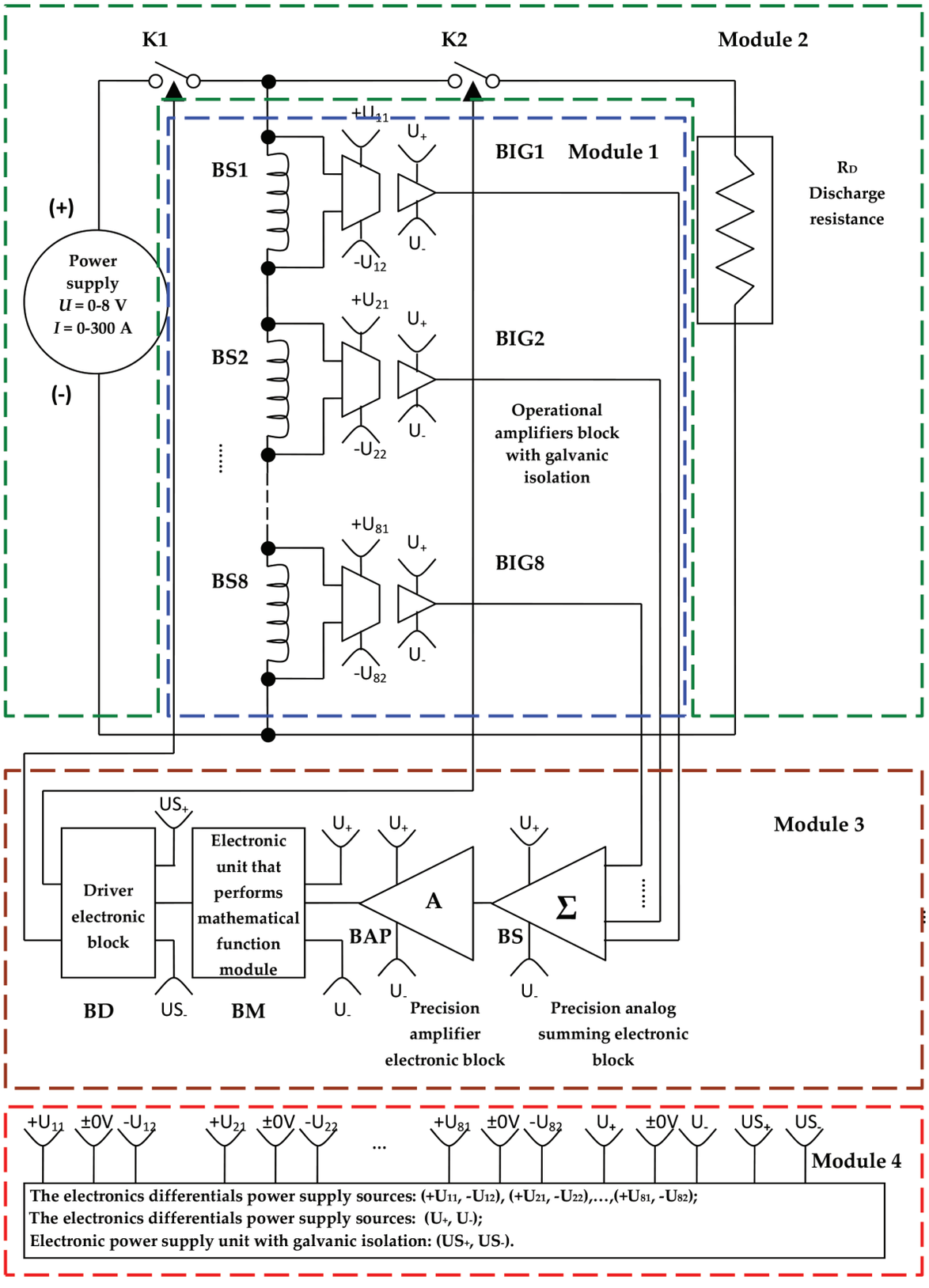


**Figure 27.** The block diagram of the experimental model of the QPS, which provides the HTS coils structures protection to quench, for the case of a variable number of HTS coils, that may form dipolar, cuadripolare, sextupolare or octupolare structures.

perform connecting and disconnecting the power source voltage and discharge resistance $R_{D,}$ respectively [17].

The first ultrafast electronic switch, *K*1, allows for powering the superconducting multipolar coils BS1, …, BS8 from the power supply voltage, in normal operation, when all the superconducting coils are in a superconducting state. Also, the first ultrafast electronic switch, *K*1, allows power supply decoupling when at least one of the multipolar superconducting coils assemblies BS1, …, BS8 was normalized.

The second ultrafast electronic switch, *K*2, allows coupling of the superconducting coils multipolar BS1, …, BS8 on a discharge resistance, $R_D$, in the case when at least one of the multipolar superconducting coils assemblies BS1, …, BS8 was normalized. Also, the second ultrafast electronic switch *K*2 allows multipolar superconducting coil BS1, …, BS8 decoupling from discharge resistance, $R_D$, in normal operation, when all the superconducting coils are in a superconducting state.

One of the important electronic modules is the precision analogue summing circuit, **Figures 27** and **28**. The precision analogue summing circuit is achieved using three analogue-integrated circuits type AMP 03, instrumentation operational amplifier from Analog Devices [18]. Each of these operational amplifiers is used in specific connection of summing [18]. At the exit $V_{OUT}$, **Figure 28**, we obtain the sum of all four signals that are applied to the inputs IN1, IN2, IN3 and IN4.

The performance of an active electronic protection system (QPS), in both cases A and B, can be evaluated by the visualization and recording of dissipated energy on the discharge resistance $R_D$, **Figures 11** and **27**, by using the system shown in **Figure 29**. When a high-temperature superconductor (HTS) coil structure that is in a superconductive state is shifting into normal conduction state (quench), the evolution of voltage drop on the superconducting coil structures will be that around the critical current, **Figure 10** and **Table 4**.

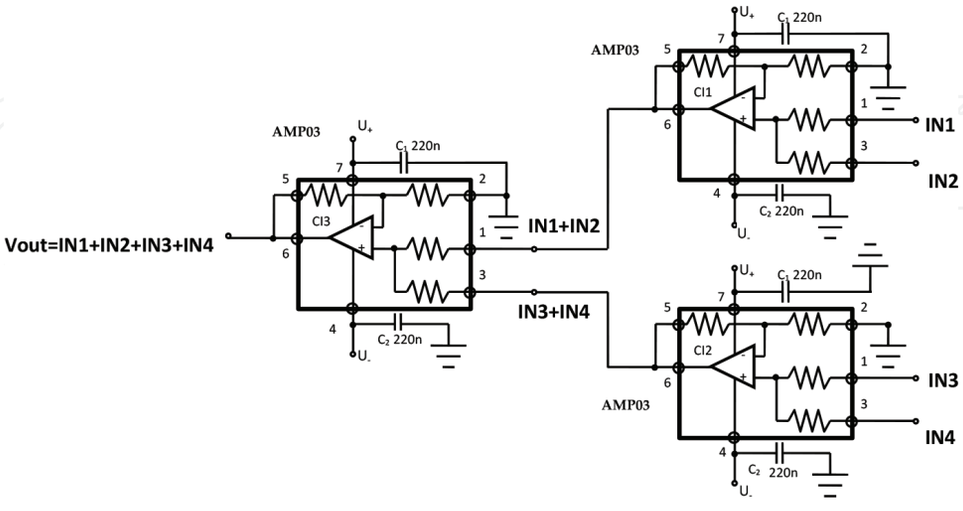


**Figure 28.** The electronic design of the precision analogue summing circuit, for the case of a HTS coils, cuadripolare structures.

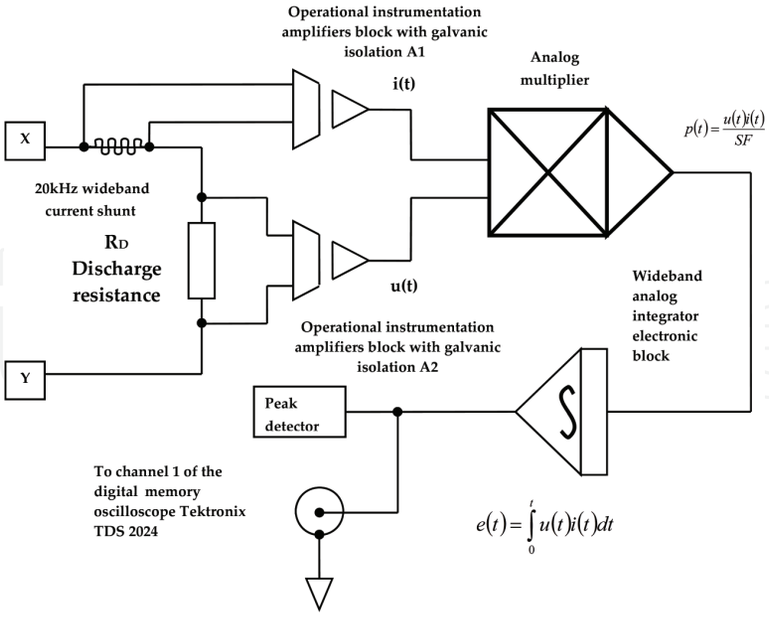


**Figure 29.** The block diagram of the measurement apparatus, which allows the visualization and recording the dissipated energy on the discharge resistance $R_{D.}$

| ***I* [A]** | ***U* [mV]** |
|---|---|
| 10 | 3.75 |
| 20 | 10.4 |
| 20 | 9.5 |
| 30 | 14 |
| 40 | 19 |
| 45 | 21 |
| 50 | 24.6 |
| 55 | 28.6 |
| 60 | 32.44 |
| 65 | 37.64 |
| 70 | 44.22 |
| 75 | 52 |
| 80 | 61.4 |
| 85 | 70 |
| 90 | 81.35 |
| 95 | 94 |
| 100 | 147 |
| 110 | 650 |
| 120 | >650 (Quench) |

**Table 4.** The voltage U picked from the superconducting coil L, versus the injected current I, at 77.46 K temperature.

http://dx.doi.org/10.5772/67854

The QPS will detect a quench situation. By multiplying the instantaneous current $i(t)$ that passes through the discharge resistance $R_D$ with the instantaneous voltage $u(t)$ from the discharge resistance $R_{D,}$ the instantaneous power is obtained, **Figure 29**. The dissipated energy on the discharge resistance $R_D$ is obtained by integrating the instantaneous power.

The YBCO tape high-temperature superconductor, with a critical temperature of 92 K, is used in the construction of superconducting coils tested. The superconducting coil structures are immersed to a cryostat filled with liquid nitrogen as cryogenic agent to decrease the working temperature of the HTS coil structures at about 77 K. Heat transfer by convection is minimized by creating a vacuum at a level of 0.001 mbar.

The experimental results confirm that the quench protection works as expected for the working conditions of the YBCO tape HTS coil structures. **Figure 30** shows the QPS of the superconducting coil during the experiments.


**Figure 30.** The experimental setup of the quench protection system of the superconducting coil during the experiments (the superconducting coil and the power supply are connected) [14].

## 3. Measurement of the electrical resistance of the sensing element as part of the resistive type gas sensors

Rare-earth oxides have been extensively explored for several advanced applications, such as in electronics, optics and heterogeneous catalysis, thanks to their peculiar properties arising from the availability of the 4f shell [19]. Ceria, either in its pure form or doped with cations $Ca^{2+}$, $Mg^{2+}$, $Sc^{2+}$, $Y^{3+}$, $Zr^{4+}$, potentially has a wide range of applications like gas sensors [20],

oxygen pumps and amperometric oxygen monitors and is adopted in three-way catalysts for reducing the emission of the toxic pollutants (CO, NO*x* and hydrocarbons, etc.) from automobile, owing to its high oxygen storage capacity, associated with its rich oxygen vacancies and low redox potential between $Ce^{3+}$ and $Ce^{4+}$. $CeO_2$ doped with rare-earth ions exhibits high oxide ion conductivity at a relatively low temperature (about 600°C) and thus has been applied in solid oxide fuel cells [21, 22]. In case of rare-earth-doped $CeO_2$, the $Y_2O_3$ (YDC) system has been studied due its relatively high electrical conductivity and the relative abundance of the yttrium element. The measured electrical conductivity value is $3.0 \times 10^{-3}$ S/cm at 500°C and $6.0 \times 10^{-2}$ S/cm at 700°C. If the sensing element is resistance, as components of the gas sensor can range from less than 100 ΩΩto several hundred of kΩ, depending on the sensing element design and the physical environment in which to be measured, you can use two main methods, as follows: measuring resistance indirectly, using a constant current source or measuring resistance using the Wheatstone bridge for which a single element varies.

### 3.1. Measuring resistance of the sensing element indirectly, by using a constant current source

If the power dissipation through the resistive sensing element is small, a technique for measuring resistance can be used, as shown in **Figure 31**. This technique consists of measuring the voltage output when a constant current is injected through the resistive sensing element, using an accurate means of measuring the voltage and an accurate current source, respectively. Thereby, any change in the current will be interpreted as a resistance change.

### 3.2. Measuring resistance of the sensing element by using the Wheatstone bridge for which a single element varies

A Wheatstone bridge measures resistance indirectly by comparison with a similar resistance, **Figure 32(a)**. In this case, all the resistances are nominally equal, but one of them (the sensing element) is variable by an amount $\Delta R$. As the equation indicates, **Figure 32(b)**, the relationship between the bridge output and $\Delta R$ is not linear. By using an instrumentation operational amplifier, (in-amps) as a Wheatstone bridge amplifier, is performed a better gain accuracy. Usually, this gain accuracy is set with a single resistor, RG and does not unbalance the bridge [23].

Excellent common mode rejection can be achieved with modern in-amps. The excitation voltage $V_B$ is typically 10 $V_{CC}$ stabilized.

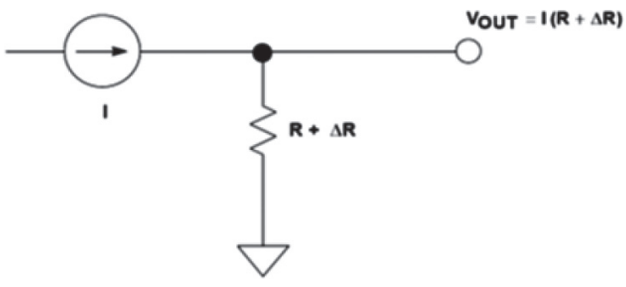


**Figure 31.** Method of indirect measurement of the resistance, using a constant current source.

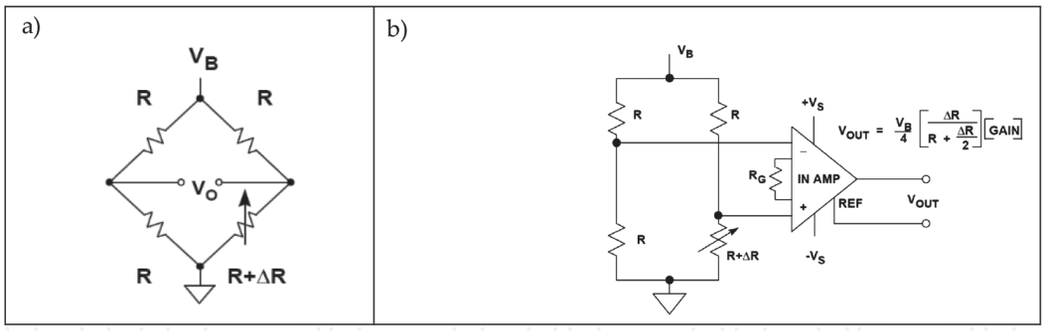


**Figure 32.** A single-element-varying Wheatstone bridge topology, which uses an instrumentation operational amplifier (in-amps), as a bridge amplifier. (a) A single-element varying Wheatstone bridge. (b) Using an instrumentation operational amplifier as a Wheatstone bridge amplifier.

## Author details

Lucian Pîslaru-Dănescu[1]* and Lipan Laurențiu Constantin[2]

*Address all correspondence to: lucian.pislaru@icpe-ca.ro

1 National Institute for Electrical Engineering ICPE-CA, Bucharest, Romania

2 University Politehnica of Bucharest, Bucharest, Romania

## References

[1] S. Moreau, M. Bergeron, and R. Clement, "COMSOL Multiphysics modeling for measurement device of electrical resistivity in laboratory test cell", *COMSOL Conference, Boston, October 13–15*, 2011.

[2] I. Lingvay, C. Lingvay, L. Pîslaru-Dănescu, and G. Velciu, "Method and Apparatus for electric resistivity measurement of the reinforced concrete structures", (in Romanian), OSIM, Patent Application *nr. A/00349/2012*.

[3] J. Molina and R. Mark Stitt, Filter Design Program for the UAF 42 Universal Active Filter, *Application Bulletin, Burr-Brown, Texas Instruments*, Tucson, AZ, PO Box 11400, AZ 85734, Street Address: 6730 S, 1993.

[4] Classic Application Notes Collection, *Analog Devices*, One Technology Way, P.O. Box 9106, Norwood, MA 02062-9106, U.S.A., 2008.

[5] ICL7107 3½ Digit LCD/LED Display, A/D Converters, *Data Sheet, Intersil*, 2005.

[6] T. Dănilă and N. Cupcea, *Operational Amplifiers* (in Romanian), Publisher Ed. Teora, Bucuresti, 1994.

[7] L. Pîslaru-Dănescu, A. M. Morega, M. Morega, and V. Stoica, "New concept of measurement apparatus for the in situ electrical resistivity of concrete structures", *8th*

*International Symposium on Advanced Topics in Electrical Engineering, ATEE 2013, 23–25 May 2013, Bucharest, Romania, Proceedings of the International Symposium on Advanced Topics in Electrical Engineering (ATEE)*, 2013. pp. 1–6, Print ISBN: 978-1-4673-5979-5, E-ISBN: 978-1-4673-5980-1, ISSN: 2068-7966, DOI: 10.1109/ATEE.2013.6563531, Accession Number: WOS:000332928500185

[8] A.M. Neville, *Properties of Concrete*, New York: Wiley & Sons, 4th Edition, 1996, ISBN 0470235276.

[9] H. Arup and O. Klinghoffer, "Junction potentials at a concrete/electrolyte interface", in *Proceedings of EUROCORR'97, Sept. 22–25, Trondheim, Norway*, 1997, vol. I, pp. 455–459.

[10] R. Myrdal, "Phenomena that disturb the measurement of potentials in concrete", in *Proceedings of Corrosion/96, paper No 339, NACE, Houston, TX*, 1996.

[11] R. Myrdal, "Potential gradients in concrete caused by charge separations in a complex electrolyte", in *Proceedings of Corrosion/97, paper No 278, NACE, Houston, TX*, 1997.

[12] T.K. Simon and V. Vass, "The electrical resistivity of concrete", Concr. Struct., 13, 2012; 61–64.

[13] Y. Yang, B. Wei, P. Chen, H. Zhang, et al., "The quench protection system for superconducting magnetic energy storage", IEEE Trans. App. Supercon., 2013; **23**: 3, DOI:10.1109/TASC.2012.2233855.

[14] L. Pîslaru-Dănescu, A. M. Morega, V. Stoica, M. Morega, and I. Dobrin, "A new electronic active system for protection to quench hazard in high temperature superconducting coils", *9th International Symposium on Advanced Topics in Electrical Engineering ATEE 2015, 7–9 May 2015, Bucharest, Romania, Proceedings of the International Symposium on Advanced Topics in Electrical Engineering (ATEE)*, 2015, pp. 692–697, ISBN: 978-1-4799-7514-3, ISSN: 2068-7966, DOI: 10.1109/ATEE.2015.7133889

[15] FUJI **VLA 517 – 01R,** *Application Manual*, Fuji Electric Co., Ltd., Electronics Group, Tokyo, Japan, 1997.

[16] L. Pîslaru-Dănescu, I. Dobrin, V. Stoica, L. C. Lipan, and I. Pisica, "Apparatus for active protection for superconducting coil at superconducting motors", (in Romanian), OSIM, Patent *nr.* 128881/2011.

[17] L. Pîslaru-Dănescu and I. Dobrin, "Active protection for superconducting multipolar coils assembly", (in Romanian), OSIM, Patent *nr. A/01004/29.11.2012.*

[18] Analog Devices, "*Precision, unity-gain differential amplifier, AMP 03*", Data Sheet, 2003, Rev. F., Norwood, MA, USA.

[19] L. Liao, H. X. Mai, Q. Yuan, H. B. Lu, J. C.Li, C. Liu, C.H. Yan, Z. X. Shen, and T. Yu,"Single $CeO_2$ nanowire gas sensor supported with Pt nanocrystals: gas sensitivity, surface bond states and chemical mechanism", J. Phys. Chem. C, 2008; **112:** 9061–9065.

[20] J. G. Li, T. Ikegami, J. H. Lee, and T. Mori, "Characterization and sintering of nanocrystalline $CeO_2$ powders synthesized by a mimic alkoxide method", Acta Mater., 2001; **49**: 419–426.

[21] H.-J. Choi, J. Moon, and H.-B. Shim, "Preparation of nanocrystalline $CeO_2$ by the precipitation method and its improved methane oxidation activity", J. Am. Ceram. Soc., 2006; **89(1)**: 343–345.

[22] J-H. Lee, J. Kim, S.W. Kim, HW. Lee, and H.S. Song, "Characterization of the electrical properties of $Y_2O_3$-doped $CeO_2$ rich $CeO_2$-$ZrO_2$ solid solutions", Solid State Ionics, 2004; **166**: 45–52.

[23] W. G. Jung, "*Operational Amplifier Application Hndbook*", Newnes, An imprint of Elsevier 30 Corporate Drive, Suite 400, Burlington, MA 01803, USA Linacre House, Jordan Hill, Oxford OX2 8DP, UK, 2005 by Analog Devices Inc., ISBN 0-7506-7844-5.

IntechOpen